Mechanical and Thermophysical Properties of 3D-Printed SiC – FY 2020

T. S. Byun
B. E. Garrison
H. Wang
A. Trofimov
T. G. Lach
C. M. Parish
M. D. Richardson
B. C. Jolly
M. Trammell
A. Schumacher
G. Vasudevamurthy
T. Koyanagi
K.A. Terrani

May 29, 2020

M2TC-20OR0403013

OAK RIDGE NATIONAL LABORATORY

MANAGED BY UT-BATTELLE FOR THE US DEPARTMENT OF ENERGY

Transformational Challenge Reactor

Mechanical and thermophysical properties of 3D-Printed SiC – FY 2020

T. S. Byun, B. E. Garrison, H. Wang, A. Trofimov, T. G. Lach, C. M. Parish,
M. D. Richardson, B. C. Jolly, M. Trammell, A. Schumacher, G. Vasudevamurthy,
T. Koyanagi, K.A. Terrani

Oak Ridge National Laboratory

Date Published: May 29, 2019

M2TC-20OR0403013

CONTENTS

FIGURES

TABLES

Mechanical and Thermophysical Properties of 3D-Printed SiC – FY 2020

ABSTRACT

In the Transformational Challenge Reactor (TCR), the fuel blocks consist of an additively-manufactured silicon carbide (SiC) matrix and uranium nitride tristructural isotropic (UN TRISO) fuel particles, which are stacked to form fuel columns. The SiC matrix is manufactured using binderjet 3D printing followed by loading the TRISO fuel particles and the chemical vapor infiltration (CVI) process. Because the fuel matrix is a primary component of the TCR core and its response to mechanical and thermal loads during operation is one of the most influential factors on the integrity of TCR core, testing and evaluation have focused on producing mechanical and thermophysical properties data for the binderjet/CVI SiC. Mechanical and thermophysical properties were measured from various types of specimens printed for two or three orientations, which included equibiaxial flexural failure strength, elastic constants, thermal diffusivity and conductivity, density, and the coefficient of thermal expansion. Flexural failure strength datasets showed similar Weibull distributions regardless of sample variants including different orientations. The mean failure strengths of the 3D-printed SiC variants were in the range of 286–306 MPa, which are 22–27% lower than that of the CVD SiC. Thermophysical test results showed that specific heat and thermal expansion are not sensitive to the build directions of SiC samples, while thermal diffusivity is highly dependent on the build direction and can be correlated to the anisotropic character of the 3D-printed SiC. This report also includes discussions on the uniaxial tensile properties of the as-printed SiC before CVI and on ongoing efforts for irradiation effects studies.

x

1. INTRODUCTION

1.1 Background

The Transformational Challenge Reactor (TCR) program seeks build the majority of the reactor core components through additive manufacturing (AM) technologies, which include the laser powder bed fusion (LPBF) of 316L stainless steel and Inconel 718 components and the combined process of binderjet 3D printing and chemical vapor infiltration (CVI) for the silicon carbide (SiC) matrix in fuel blocks [1,2]. For the TCR core, the performance of the SiC fuel matrix is particularly important as it occupies the largest volume among the solid structures and needs to demonstrate good structural and thermal behaviors as a fuel matrix and structure, an additional barrier to radionuclide release, and a heat transfer medium. A streamlined novel methodology for the production of carbide ceramics was developed recently under the TCR program [2] and is being leveraged to produce the fuel matrix for the TCR core; however, detailed evaluation of the binderjet/CVI SiC materials produced by the new processing route is needed to inform high fidelity reactor design and analysis as well as material qualification activities.

Many past studies have demonstrated the excellent high temperature properties of SiC materials, such as high strength, creep resistance, and oxidation resistance [3–5]. In particular, their high radiation tolerance makes them optimal materials for some nuclear structural components [3]. The quality of SiC for nuclear power applications greatly depends on purity, crystallinity, and grain boundary state [4,5]. Several manufacturing techniques are used to produce high-quality, high-density SiC matrices, including chemical vapor deposition (CVD) [6], nano-infiltration transient eutectic (NITE) processing [4], or CVI [7] of high purity SiC often on highly pure SiC substrates or fibers. The CVD of SiC is a bulk SiC processing technique that produces highly pure SiC [2,8].

Unlike the high temperatures needed for sintering of generic SiC or even the NITE process [4,9,10], the CVI process only requires a temperature of about 1000–1200°C and is thus considered a low temperature processing route [7]. This is important for processing TCR fuel blocks with high precision as the dimensional distortion in an as-printed fuel basket is limited in such a low-temperature regime. The primary issue with the CVI processing may be the inherent porosity that forms as infiltration can prematurely close off open pores, with porosity as high as 20% or more in some fiber/matrix composites; this porosity correlates directly with reductions in thermal conductivity and strength. The CVI-SiC produces the highest quality matrix material with high purity and full crystallinity and is thus often considered the reference material for nuclear-grade SiC-based materials [3,7].

Building on the work of past CVI technology, a preferable option for additive manufacturing of SiC structural components is the formation of a green compact of micro-scale SiC particles by AM binderjet printing followed by densification by CVI, which is a process successfully developed at Oak Ridge National Laboratory (ORNL) as part of the TCR program [1,11]. This process is desirable for the TCR program because of its ability to make complex shapes such as the fuel baskets with detailed features for effective coolant flow and containing TRISO fuel

particles. Some basic properties of these particle/matrix composites have been studied in the unirradiated state [2]. Relative to the CVI fiber/matrix composites, the porosity produced here is about 8-10% which is on the lower end found in CVI processing. Post-irradiation examination (PIE) and testing has yet to be performed, though the lack of any interphase layers and the high purity and fully crystalline microstructure is expected to provide good radiation tolerance [2].

This research aimed to build up mechanical and thermophysical properties data for the SiC processed via binderjet printing with and without CVI. Mechanical and thermophysical properties were measured from different types of specimens printed for two or three orientations, which included equibiaxial flexural and tensile failure strengths, thermal diffusivity and conductivity, density, and the coefficient of thermal expansion. Currently, six irradiation capsules containing this 3D-printed SiC have completed irradiation testing at ORNL's High Flux Isotope Reactor and are awaiting PIE while other irradiation tests are planned. Along with the extended set of results to be obtained after irradiation, the dataset reported here will provide a materials property database for materials qualification and core structure design and analysis.

1.2 Document Purpose and Applications

The purpose of this document is to quantify and summarize mechanical and thermophysical property data on SiC produced using an advanced manufacturing approach, which consists of a combination of binderjet printing and chemical vapor infiltration (CVI) to derive high purity and fully crystalline material. The additively manufactured SiC is the most important core material in the TCR as it is the matrix material containing the TRISO fuel particles. This document is intended for use by the core component manufacturers, modelers, and reactor designers in TCR program and by other researchers.

This document is primarily intended to inform the TCR design community on the material performance of candidate materials and manufacturing processes, but it can also be used for future reactor designs or applications for which the materials and manufacturing processes presented within are of interest.

2. BUILDS OF MATERIALS AND SPECIMENS

2.1 A Combined Process of Binderjet Printing and CVI

Binder jet 3D printing followed by a densification process is a unique technology that is performed at near room temperature and therefore is highly agnostic to the feedstock powder. A novel methodology for the production of carbide ceramics was developed recently and is being leveraged to produce a ceramic inert fuel matrix or structures for the TCR core [1,2]. Specimens used for this testing and characterization task were produced using the newly established manufacturing processes.

The properties of the SiC materials described in this document are for those derived from α-SiC (hexagonal phase) feedstock powder with ~20 μm in diameter from Sigma Aldrich with a purity >99.5%. The Innovent binderjet printing systems from ExOne Company (North Huntingdon, PA) were used to produce the test specimens. An aqueous binder (Binder 05 from ExOne) was used during printing that underwent curing at 190°C for 6 h in air. The curing step drives off the majority of the aqueous binder, and the binder is almost entirely decomposed and dissociated away from the part during the next step of the process at a higher temperature.

After the green parts are binderjet printed and cured, they are transferred to the furnace for chemical vapor infiltration (CVI) process where they undergo densification. A mixture of H_2 gas and methyltrichlorosilane (MTS) carrier gas is injected into the CVI furnace to decompose the gases at about 1000 ºC and deposit high-purity, stoichiometric, and crystalline SiC around the 3D-printed SiC powder particles. Depending on the size of each part and the processed batch, the CVI process can take hours to days to close the open porosities.

2.2   Builds of SiC Specimens

Various types of specimens have been printed using the combined binderjet and CVI processing. First, a large number of mini-disk (6 mm diameter × 0.5 mm thickness) specimens were produced for baseline and post-irradiation tests. The baseline tests for both mechanical properties and thermophysical properties have been completed and the results are presented in this report. Second, two sizes of flat tensile specimens were produced via binderjet printing and tensile-tested without CVI densification. This was to investigate the properties of intermediate material in the processing which can provide information on handling and process design. Third, rodlet samples with three different directions were produced to measure the coefficient of thermal expansion in those directions. Fourth, the 12.7 mm diameter, 1.59 mm thick disks were produced to measure elastic constants using a resonant ultrasonic spectroscopy technique.

Table 1 lists the types of test specimens, along with information on their orientations, build identifications, and purposes. The build identification numbers (or run dates) can be used to revisit detailed printing and CVI conditions. Figure 1 explains the orientation relationship in the printing: Among the disk specimens, the XY series specimens are printed on XY plane, and the Z specimens are printed in the Z (edge-on view) direction. The rod-type specimens are built along X, Y (binder deposition) and Z (layer stacking) direction. Some specimens that are characterized as "Si-doped" contain a small volume fraction (< 3%) of free Si in their microstructure. TCR targets use of Si-free 3D-printed SiC by slightly elevating the temperature during the CVI process. Nonetheless, both 3D-printed SiC variants (with and without residual free Si) are examined in this study to provide a complete analysis.

Table 1. List of specimen builds for testing and evaluation

Specimen Type	Build I.D./Run Date	Sample Orientation	Processing	Purpose	Remarks
Mini-disk: Ø6 mm X 0.5 mm	LSCVI19	XY*	Binderjet Printing + CVI	Equibiaxial flexural strength test Thermal diffusivity measurement Irradiation effect testing	Si-doped
	LSCVI29: 20191004-1-1 20191004-1-2	XY*			
	LSCVI31	Z			Edge-on
Flat tensile specimen	20191017 Innovent	X, Y (GL=5 mm)	Binderjet Printing (no CVI)	Uniaxial tensile test	Green SiC
	20191106 Innovent+	X, Y (GL=5 mm)			
	20190726 20191017 20191018 Innovent	X, Y (GL=15 mm)			
	20191017 20190807 20191104 20191105 20200227 20200228 Innovent+	X, Y (GL=15 mm)			
Mini-rodlet: Ø6 mm X 10 mm	20200316-2-1 (X) 20200317-2-3 (X) 20200316-2-2 (Y) 20200316-2-3 (Z) 20200317-2-1 (Z)	X, Y, Z	Binderjet Printing + CVI	Coefficient of thermal expansion test	
Disk: Ø12.7 mm X 1.59 mm	20200331-2-3 20200401-2-2 20200401-2-3	XY*	Binderjet Printing + CVI	Elastic constants	Used in strength calculation

*Note: *Layer (on XY plane) stacking in the Z-direction; X, Y, Z – sample growth directions; GL=gage section length; Innovent and Innovent+ indicate the old and new printers, respectively.*
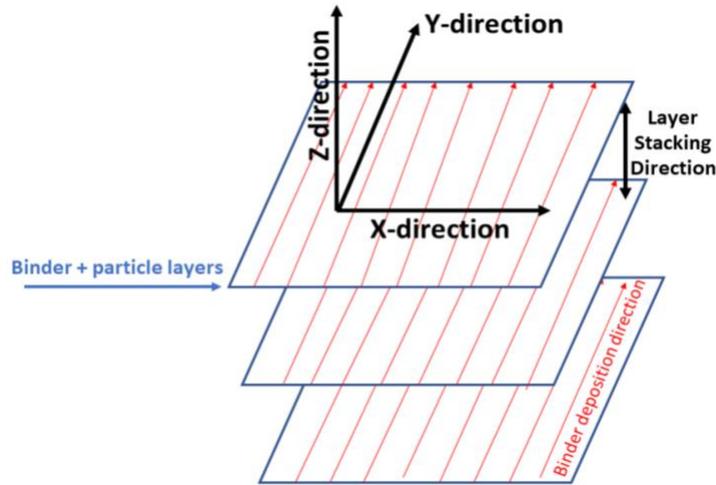
Figure 1. Schematic of orientation relationship in binderjet printing.

3. MECHANICAL PROPERTIES

Mechanical testing has been performed primarily to establish the baseline mechanical properties of the additively manufactured SiC materials with different orientations. Mechanical testing after neutron irradiation at the High Flux Isotope Reactor (HFIR) will be performed later in the coming months under the TCR program [12], and the results will be compared with the datasets presented in this document. The two following sections present results of the equibiaxial flexural strength test for the SiC specimens after combined processes of binderjet printing and CVI and the uniaxial tensile testing for the as-printed SiC before CVI. Both datasets are analyzed with Weibull statistics.

3.1 Failure Strength of 3D-Printed SiC after CVI

3.1.1 Equibiaxial Flexural Strength Test

A miniaturized equibiaxial flexural strength test method was used to measure the fracture strengths of SiC materials using thin disk (0.5 mm thickness × 6 mm diameter) specimens. In testing a disk specimen is loaded up to fracture in a concentric ring-on-ring loading mode, as shown in Figure 2. This can induce a relatively uniform biaxial tensile stress on the lower surface of disk specimen; specimen fracture occurs when the tensile stress at the weakest point in the surface layer reaches a critical level. This method is described in the ASTM standard test method C1499-09 [13]. Table 2 lists all 84 specimens tested and analyzed in this baseline property evaluation task.
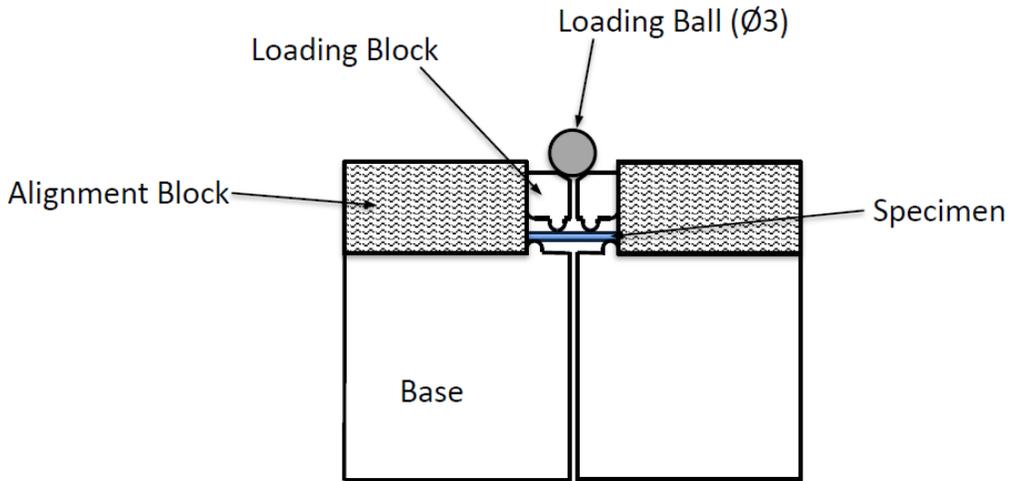
Figure 2. Schematic section view of fixturing and test specimen for equibiaxial flexural strength testing. Note that the diameters of upper and lower contact rings are 2 mm and 5 mm, respectively.

For the biaxial flexural testing, an MTS Insight Electromechanical Testing System with a 2 kN loading capacity in Building 4508, Low Activation Materials Development and Analysis (LAMDA facility), was used (note that the same system will be used for the specimens after irradiation). The maximum load obtained in each test under monotonic application of load, practically the fracture or breaking load, is converted to the fracture stress at the surface of disk specimen (σ_f). The disks were 6 mm in diameter and 0.48 mm thick on average. The measured thicknesses of the individual specimens were used in calculation. The formula for the equibiaxial fracture strength, σ_f, of a circular plate specimen in units of MPa is given by [13]

$$\sigma_f = \frac{3F}{2\pi h^2}\left[(1-v)\left(\frac{D_S^2 - D_L^2}{2D^2}\right) + (1+v)ln\left(\frac{D_S}{D_L}\right)\right], \qquad \text{(Equation 1)}$$

where
F = the breaking (fracture) load [N],
h = the thickness of thin circular specimen [mm],
D = the diameter of circular test specimen [6 mm],
D_S = the support ring diameter [2 mm],
D_L = the load ring diameter [5 mm], and
v = Poisson ratio.

Table 2. List of disk specimens for flexural strength tests

CVD SiC		3D SiC-XY		3D SiC-Z		3D SiC-XY-Si	
Specimen ID	Thickness (mm)	Specimen ID	Thickness (mm)	Specimen ID	Thickness (mm)	Specimen ID	Thickness (mm)
C052	0.49	XY001	0.49	Z010	0.50	XS03	0.47
C053	0.49	XY003	0.47	Z016	0.49	XS05	0.48
C054	0.48	XY008	0.49	Z017	0.49	XS10	0.46
C055	0.48	XY009	0.49	Z019	0.49	XS11	0.47
C056	0.49	XY011	0.49	Z046	0.48	XS12	0.46
C057	0.48	XY012	0.48	Z051	0.47	XS13	0.45
C058	0.48	XY013	0.49	Z053	0.49	XS15	0.47
C059	0.49	XY014	0.48			XS16	0.44
C060	0.49	XY015	0.48			XS17	0.45
C061	0.49	XY017	0.49			XS18	0.45
C062	0.49	XY019	0.48			XS19	0.46
C063	0.48	XY020	0.49			XS20	0.46
C064	0.48	XY022	0.49			XS41	0.48
C065	0.49	XY023	0.49			XS42	0.49
C066	0.49	XY027	0.48			XS43	0.49
C067	0.48	XY029	0.49			XS44	0.48
C068	0.49	XY032	0.49			XS45	0.48
C069	0.49	XY034	0.49			XS46	0.47
C070	0.49	XY037	0.47			XS48	0.48
C071	0.49	XY042	0.48			XS49	0.49
C072	0.49	XY043	0.48			XS50	0.47
C073	0.49	XY044	0.48			XS51	0.47
C074	0.49	XY048	0.48			XS52	0.46
C075	0.49					XS53	0.47
C076	0.48					XS54	0.47
C077	0.49					XS55	0.47
C078	0.49					XS59	0.47

3.1.2 Equibiaxial Failure Strength of SiC

The failure strength of 3D-printed SiC for the fuel matrix, a key TCR core structural material, is of great importance to the structural integrity of the core. Because the binderjet SiC materials with or without CVI are brittle materials, their failure strength is controlled by the cracking strength of the "weakest link," i.e., fracture occurs at the largest flaw present in the sample. This type of behavior is well described by Weibull statistics [14], in which crack-initiating flaws are assumed to be randomly distributed throughout the tested volume. Because the same volume specimens are tested for each batch of specimens, the cumulative distribution function or probability of failure for the Weibull distribution is expressed by

$$P_f(\sigma_f) = 1 - e^{-(\frac{\sigma_f}{\sigma_0})^m},$$
(Equation 2)

where m is the Weibull modulus and σ_0 the characteristic strength or scale parameter. The two parameters in the function, m and σ_0, are also called the shape and scale parameters, respectively. The probability of failure is calculated by $P_f = (i-0.3)/(N+0.4)$ where i is the rank of failure strength in a set of N data. These results may be extended to predict failure probability in larger geometries by normalizing against the volume or surface area of these tests (i.e., 1.57 mm^3 and 3.14 mm^2).

The probability of failure data for the 3D-printed SiC with CVI are plotted in Figure 3, along with the data for CVD SiC tested in this same study as the reference material. These plots indicate that the characteristic strength of the three 3D-printed SiC variants is approximately 20% lower than the CVD SiC. Similar failure probability behaviors are observed for the three 3D-printed SiC variants although the data for the 3D-printed SiC with XY orientation show slightly higher probability of failure in the low failure strength region (< ~310 MPa). Comparison of these failure strength data also indicates that neither the effect of specimen orientation (XY versus Z) nor the effect of Si doping (in 3D-XY-Si) significantly affects the probability of failure behavior in the 3D-printed materials. It is also observed that the probability of failure curve for the CVD SiC extends to the strength region of the 3D-printed SiC samples (< 300 MPa), although its overall strength is clearly higher than its printed SiC counterparts.
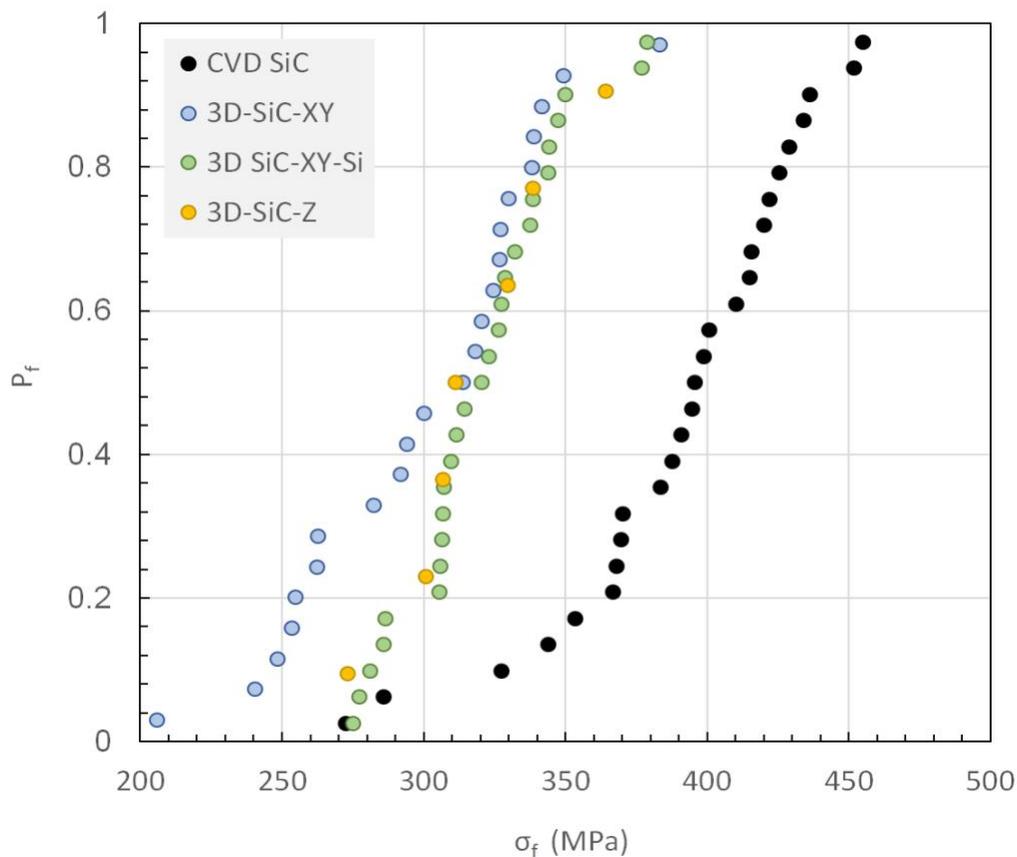
Figure 3. Plots of failure probability (P_f) versus failure strength data (σ_f) from monotonic equibiaxial flexural strength testing.

The two parameters in Equation 2, m and σ_0, can be decided by plotting the data as a log-log graph or so-called the Weibull plot using:

$$Ln(-Ln\,(1 - P_f)) = m \times Ln(\sigma_f) - m \times Ln(\sigma_0) \qquad \text{(Equation 3)}$$

The Weibull plot has special scales that are designed such that the points will be linear if the failure strength data follow a Weibull distribution or are from one failure mechanism. The least squares fit of this line yields estimates for the shape and scale parameters of the Weibull distribution. Figure 4 compares the Weibull plots for the 3D-printed SiC and CVD SiC, where all datasets fit reasonably well in respective regression lines. The Weibull parameters determined by the regression lines are summarized in Table 3. The Weibull moduli measured are within the range of 7 to 14, which is a typical range for SiC materials [15–17], and no evidence of a clear difference between the binderjet plus CVI processed SiC and the reference CVD SiC is found. Similar to the difference found in the failure load data in Figure 3, the mean characteristic strength of the 3D-printed SiC is 22–27% lower than that of the CVD material (~390 MPa).
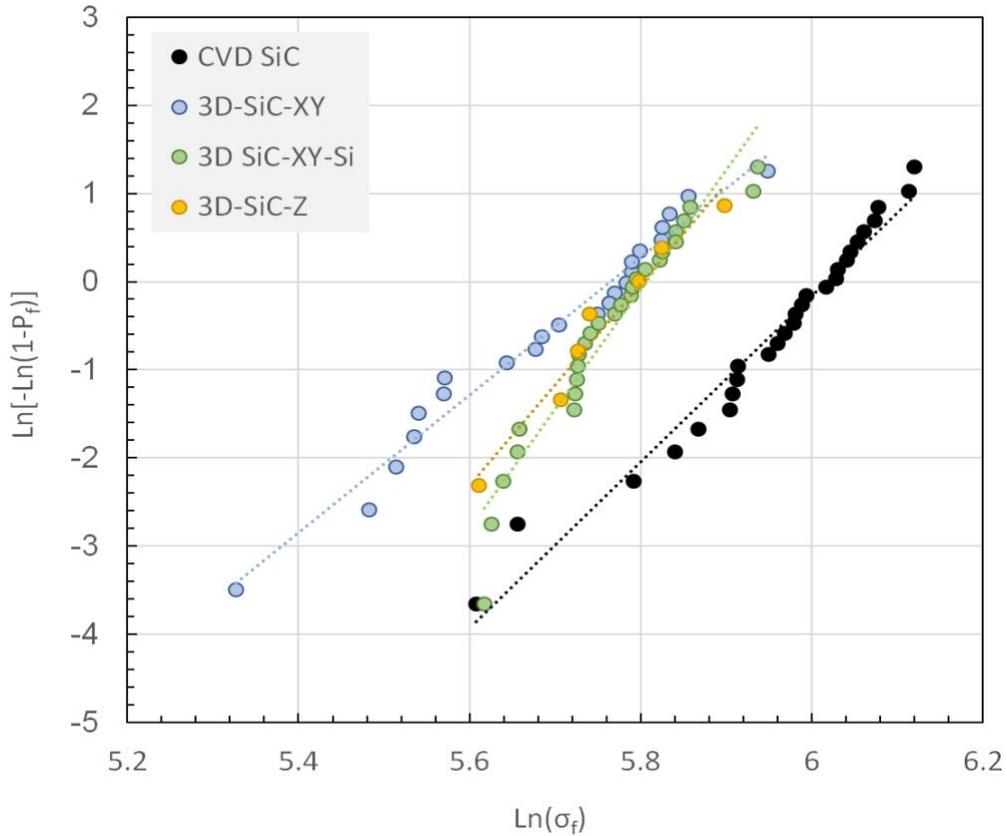
Figure 4. Weibull plots of SiC failure strength data from equibiaxial flexural strength testing.

Table 3. Summary result of Weibull statistics analysis for equibiaxial flexural strength tests

Materials	Specimen I.D.	Dimension	Weibull Modulus (=m)	Scale Parameter (=σ_0) (MPa)	Mean Failure Strength (MPa)
CVD SiC	C0i (i=1-27)	Ø6 mm x 0.487 mm	9.41	404.3	389.8
3D-SiC-XY	XYi (i=1-23)	Ø6 mm x 0.484 mm	7.81	318.9	286.3
3D SiC-XY-Si	XSi (i=1-27)	Ø6 mm x 0.469 mm	13.56	332.5	302.9
3D-SiC-Z	Zi (i=1-7)	Ø6 mm x 0.487 mm	11.43	331.0	305.3

Although the multiple types of flaw distributions or simultaneous occurrence of volume and surface defects can initiate cracks, the role of flaws and pores in the surface layer should be dominant in the failure of these SiC disks under the present equibiaxial bend loading. The relatively monotonically linear shapes of the Weibull plots indicate that the cracking mechanism, most likely initiating from the specimen's lower surface where the maximum tension stress occurs, does not change in each set of specimens. Finally, it should be also noted that the flexural failure strength is dependent on the Poisson's ratio (v) of the test specimen, as indicated in Equation 1. A newly measured Poisson's ratio (0.124) was used for the 3D printed SiC specimens and a higher value (0.21) for the CVD SiC. Therefore, the lower failure strengths measured from the 3D-printed SiC materials are partially due to their lower Poisson's ratio.

3.2 Uniaxial Tensile Strength of As-printed SiC before CVI

Uniaxial tensile testing of the intermediate or green SiC material—the binderjet-printed SiC before CVI process—was performed to evaluate its mechanical behavior. Although the mechanical properties of these specimens are not directly relevant to SiC performance in the TCR, it is important to know the strength of the green material because they undergo handling during the fuel manufacturing process and will need reasonable mechanical strength. The test result will also provide valuable feedback to help in understanding the details of binderjet processing.

3.2.1 Specimens and Testing

In green SiC before CVI, the bonding strength from the cured residue of binder may carry the majority of the applied stress, and the mechanical behavior of such materials will be highly dependent on the orientation of specimen in relation to the loading direction. The main interest in this work, therefore, was to determine the difference in the mechanical properties of the parts with different orientations. Because the green SiC specimens are fragile and must be handled very carefully, shoulder loading through a polyurethane blanket layer in a metallic grip was used in testing the dog-bone-type tensile specimens. The geometries chosen are shown below in

Figure 5. Two (smaller and larger) geometries were chosen to investigate the size effect in the statistics of failure strength data; their gage section volume ratio is about 37.5. This size range might also be desirable to simulate the failure behavior relevant to that of the TCR fuel baskets.
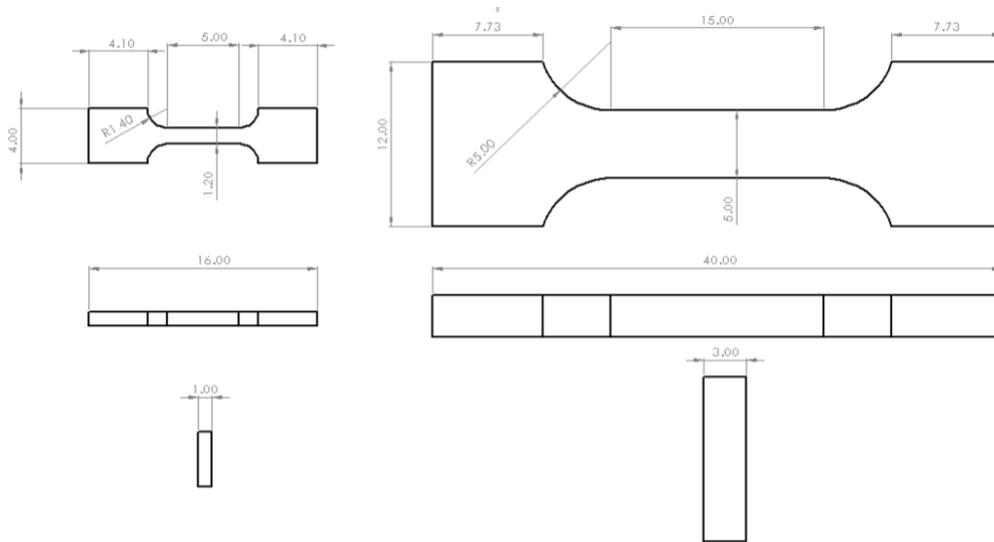
Figure 5. Drawings of the smaller (left) and larger (right) geometry of 3D-printed SiC shoulder-load tensile specimens. All dimensions are in mm.

Tensile tests were performed in an MTS Insight electromechanical system with a 100 N load cell. Specimen images and geometry measurements were taken on a Keyence VR-5000 microscope. The SiC tensile specimens with the uniaxial loading direction parallel to the roller (x-direction) and the binder deposition (y-direction). As in the above section 3.1, the failure strength data were analyzed using 2-parameter Weibull statistics model.

3.2.2   *Surface Profile Image*

Surface roughness images from four specimens printed in the x- and y-directions are displayed in Figure 6. It is observed that the printer's deposition process, which is performed by rows of nozzles that leave visible artifacts or striations along their movements. These rows of small bumps are expected to impact mechanical performance by introducing aligned pores and/or defects.

Nonuniform features are also found in each specimen. In some samples the striated feature is more prominent in only part of the specimen, while portions of other samples show buildup, as seen in the top area of the first specimen and in both head sections of the third specimen. Because these features appear to leave a wake which progresses along the roller direction, they are believed to be caused by friction between the roller and powder/binder mixture. To reduce the probability of this occurring, the drying time and the amount of powder dropped per layer

were increased. Both these nonuniform features are expected to impact mechanical test results by producing undesirable stress concentrations. Fortunately, the TCR Digital Platform continuously monitors the build process and is able to identify these types of features and flaws during manufacturing and establish a correlation between their occurrence and mechanical performance.
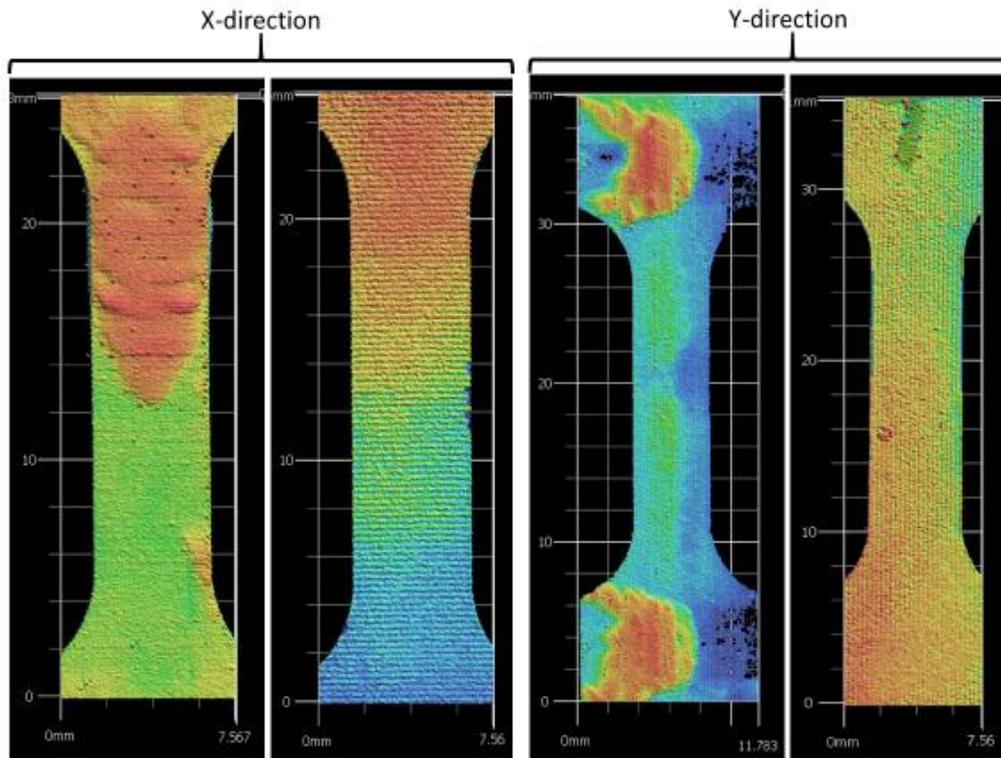
Figure 6. Surface profile images of four different tensile specimens showing printing striations along deposition (Y) direction and different buildups in the roller (X) direction.

3.2.3   Uniaxial Failure Strength of Green SiC

The probability of failure versus failure strength data for the 3D-printed SiC materials before CVI is plotted in Figure 7. An obvious observation is that the green SiC tensile bars printed in the y-direction are two to five times stronger than their x-direction counterparts. Regardless of different specimen sizes and printers, the effect of specimen orientation is dominant in the distribution of failure strength data and the datasets from x-direction specimens are clearly shifted to the lower strength region. It is also observed that the size effect from the difference in gage section size ($5\times1.2\times1$ mm$_3$ versus $15\times15\times3$ mm$_3$) is more pronounced among the datasets of the y-direction specimens. The less obvious size effect in the datasets of the x-direction specimens might be because other factors become more dominant in the lower strength range such as power material and printing conditions.

Such an obvious orientation dependence of failure strength can be well explained by the surface profile images in Figure 6. As the bonding across the printing striations is obviously weaker than that along the row feature, applying a load in the x-direction or perpendicular to these striations might cause a failure at a relatively lower stress. Furthermore, the nonuniform build features on specimen surfaces may explain why relatively lower slopes from the smaller specimens are observed because the same degree of surface nonuniformity has a greater effect on the scattering of strength data.
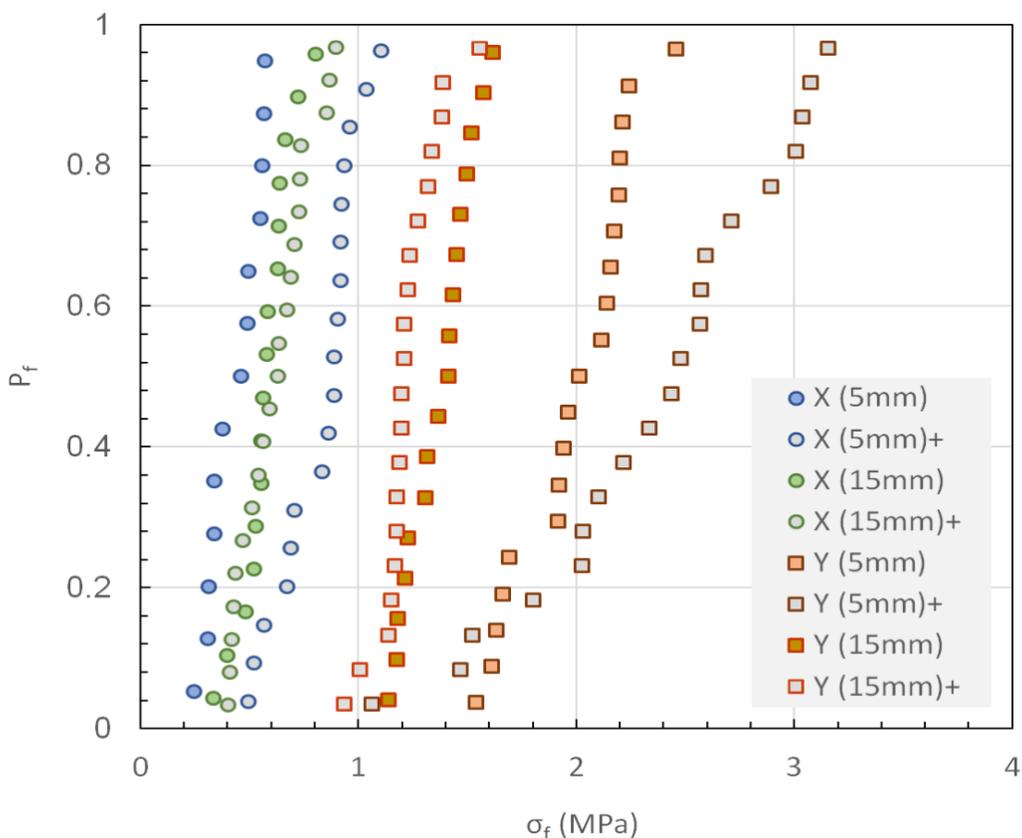
Figure 7. Plots of failure probability (P_f) versus failure strength data (σ_f) from uniaxial tension testing (+indicates the specimens were printed using the new Innovent system)

The results from the two-parameter Weibull statistics analysis are shown in Figure 8, and the Weibull parameters determined from the analysis and the mean strength values are summarized in Table 4. A wide range of Weibull moduli, within 3–11, is calculated from the tensile test datasets, among which the relatively lower moduli ($< {\sim}5$) are usually found from very small SiC samples [16,17]. It is noted that the Weibull moduli of the y-direction specimen sets are 2.0 to 2.5 times that of their x-direction counterparts for three of the four pairs. The ratios between corresponding strength parameters are in similar ranges.

13
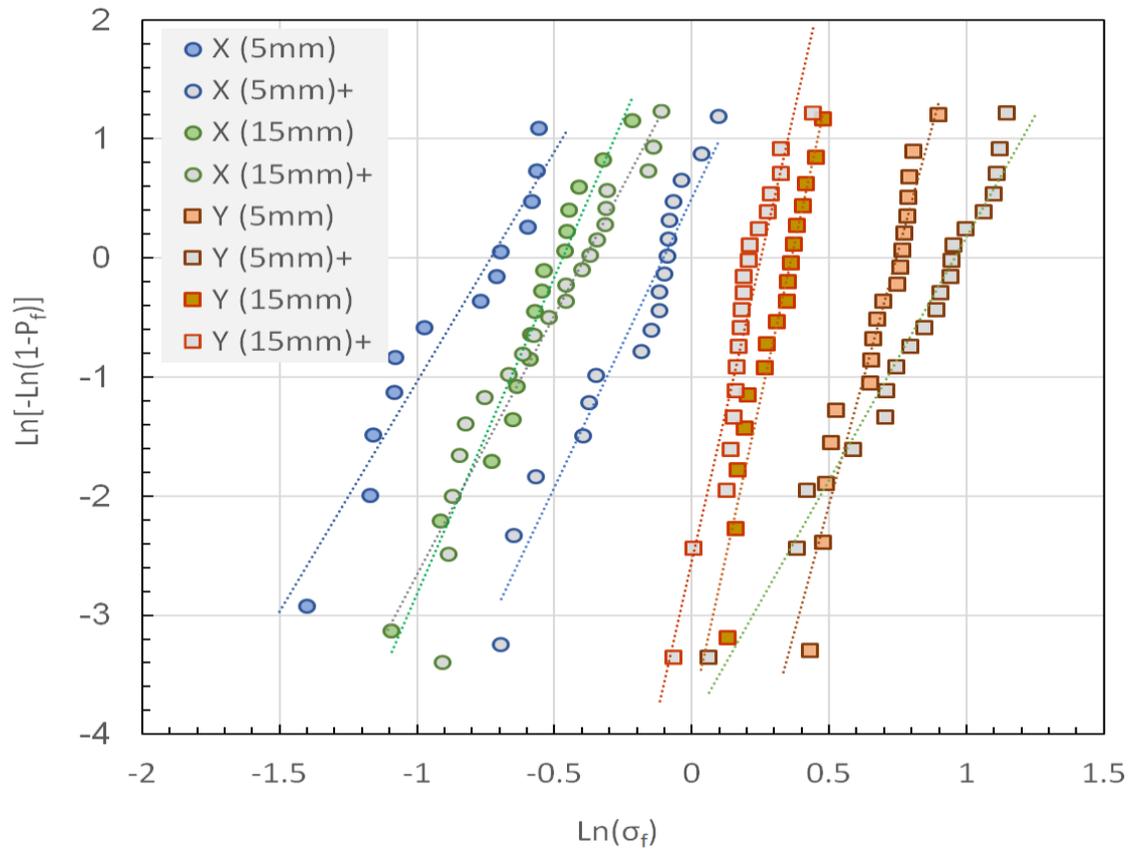
Figure 8. Weibull plots for eight failure strength datasets from as-printed SiC specimens.

Table 4. Summary result of Weibull statistics analysis for uniaxial tensile tests

Specimen Size (Gage Section Dimension)	Orientation/ Printer	Sample Size (=N)	Weibull Modulus (=m)	Scale Parameter σ_0 (MPa)	Mean Failure Strength (MPa)
Large (15x5x3 mm)	X/Innovent	16	5.31	0.63	0.58
	Y/Innovent	17	10.44	1.44	1.37
	X/Innovent+	21	4.35	0.68	0.62
	Y/Innovent+	20	10.12	1.29	1.23
Small (5x1.2x1 mm)	X/Innovent	13	3.87	0.48	0.43
	Y/Innovent	19	8.45	2.11	1.99
	X/Innovent+	18	4.85	0.90	0.83
	Y/Innovent+	20	4.09	2.60	2.36

Images of three failed tensile specimens are shown in Figure 9, which showing that failure occurred in the gage section, at the shoulder, or through split of layers, respectively. In fact, specimen failure quite often occurred at the shoulder location instead of the gage section, which was more common in the stronger y-direction specimens. This might have been caused by the unbalanced shoulder curvature produced by inaccurate nozzle stops for forming the curvature. In contrast, the x-direction specimens exhibited a more common failure in the gage section but at much lower stresses overall. It is likely that this was caused by a stress concentration from the rows of defects created by the binder rows. Finally, the layer failure in Figure 9(c) is caused by the weakest bonding in the layer-stacking (Z) direction. For a similar reason, the testing of specimens printed in the z-direction was attempted but suspended. This was because they often could not withstand the weight of the tensile fixture or low level of preload, which would produce unreliable results. This may suggest that applying any significant load in the z-direction should be avoided when handling green SiC components.
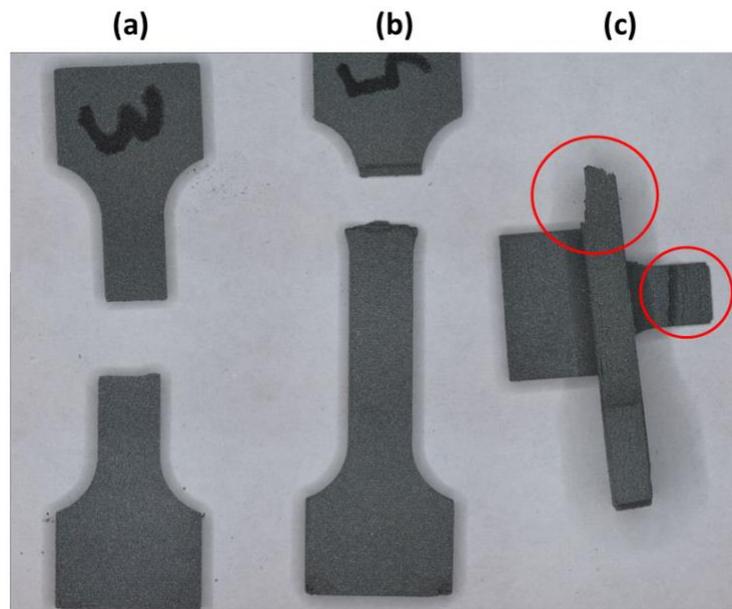
Figure 9. Image of the failure locations: (a) at the gage section, (b) at the shoulder, (c) through the layers. Through the layers refers to when the crack propagates between printed layers in parallel to the uniaxial direction.

4. THERMOPHYSICAL PROPERTIES

A series of measurements were carried out to obtain datasets for thermophysical properties of 3D-printed SiC. The results will be used in core design as well as for baseline property data for the post-irradiation test data. Samples were prepared to measure (1) thermal diffusivity, (2) density, (3) the coefficient of thermal expansion (CTE), and specific heat (Cp). Shown in Figure

10 are the three main pieces of equipment used to take these measurements. The following sections describe the experimental details and results.

Figure 10. From left to right: laser flash system for thermal diffusivity, differential scanning calorimeter (DSC) for specific heat (C_p) and thermal expansion coefficient (CTE) testing systems.

4.1   Thermal Diffusivity

Thermal diffusivity of 6 mm diameter $\times$ 0.5 mm thick SiC disks was measured using a laser flash system, Netzsch LFA457 Microflash, shown in Figure 1. A laser flash system, Netzsch LFA457 Microflash, shown in Figure 1, was used. The test follows ASTM E1461-07 [18] and used a Nd:Glass laser (λ = 1.06 μm) to deposit a heat pulse (600 μs) to the back surface of a sample. An infrared detector (InSb: λ = 3–5 μm) was used to record the top surface temperature transient through a sapphire window. The half-rise time ($t_{1/2}$) was determined by software, and thermal diffusivity (α) was calculated using the Parker's [19] equation, assuming no heat loss:

$$\alpha = 0.139d_2/t_{1/2}, \hspace{3cm} \text{(Equation 4)}$$

where d is the specimen thickness. In practice, a heat loss correction using the Cowan method [20] or Clark & Taylor [21] analysis is applied along with pulse-width correction. The diffusivity tests were performed under argon purge gas from ambient (23 °C) to 900 °C in 100 °C steps. Three measurements were taken at each set temperature.

Plots of thermal diffusivity versus temperature are shown in Figure 11. The Z series has the highest room temperature value of 25 mm$_2$/sec, the XY samples have a value of 15 mm$_2$/sec and the Si-doped XS samples (printed on X-Y plane) have the lowest value of 10 mm$_2$/sec. As a reference, the thermal diffusivities of SiC at room temperature for fully dense 3C, 4H and 6H SiC are 160, 170 and 220 mm$_2$/sec, respectively [22]. In sintered SiC materials, their microstructural features, specifically grain boundaries and defects, play important roles in scattering phonons, and hence their thermal diffusivities at room temperatures are in the range of

16

50-80 mm2/sec, typically lower than those of fully dense SiC materials. In the 3D printed SiC materials, however, their porosity results in relatively lower thermal diffusivity. Even after CVI process, the pores are not completely filled with SiC, and therefore the microstructures of these materials still have more defects to scatter phonons. After irradiation, irradiation-induced defects will reduce the thermal diffusivity of SiC-based materials. This reduction will be more significant in materials with a higher starting thermal diffusivity. Therefore, it is expected that although all the materials will experience a reduction in their thermal diffusivity after irradiation, the difference in thermal diffusivity between the 3D-printed SiC and reference CVD SiC will be smaller.

Among the 3D-printed materials, the microstructural differences in the different series result in anisotropy in heat conduction. Thermal diffusivity values of all three series decrease with increasing temperature, which is typical for lattice thermal conduction of ceramics (Umklapp scattering). The differences in the three principal directions are consistent with the 3D-printing build directions and the resulting microstructures. During cooling, measurements were taken at 300 °C and 100 °C for all specimens. There were no observable changes in the measurements, which indicates that all three SiC materials were stable after heating to 900 °C.
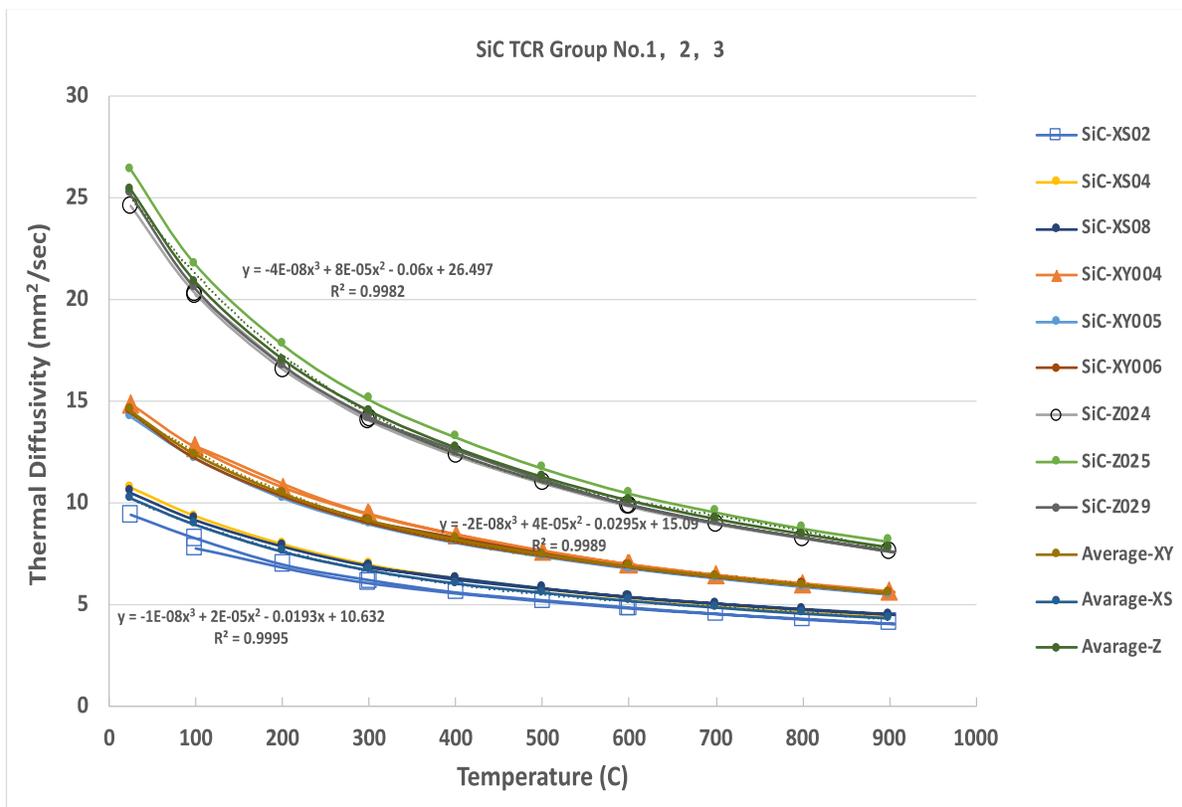

Figure 11. Thermal diffusivity of 3D-printed SiC after CVI in three orientations.

17

Thermal diffusivity data of the three series were averaged using the three duplicates and shown as averages for each series. A simple 3rd-order polynomial curve fit was used:

$$Thermal\ Diffusivity = A + BT + CT^2 + DT^3 \qquad\qquad \text{(Equation 5)}$$

where T is temperature in °C. Curve fit parameters are shown in Table 5. They are empirical equations for values between 23–900 °C.

Table 5. Curve fitting parameters in the thermal diffusivity equation for the XS, XY, and Z series specimens

Series I.D.	A	B	C	D
XS	10.632	-0.0193	2.369E-5	-1.120E-8
XY	15.090	-0.0295	3.705E-05	-1.792E-08
Z	26.497	-0.0600	7.676E-05	-3.724E-08

4.2   Density Evaluation

The density of the SiC specimens was measured using the mass and volume of the thermal diffusivity samples. Because the measured dimensions of the miniature disk samples are thought to include errors, the density data presented are not highly accurate, although they can clearly show the difference from processing routes.

As shown in Figure 12, nine 3D-printed specimens showed scatter from 2.75 g/cm³ to 2.94 g/cm³ which is 85.7% to 91.6% of the theoretical density of 3.21 g/cm³. The average value was 2.86 g/cm³ (89% dense). The scatter was also due the small size of the specimens (6 mm diameter, 0.5 mm thick). In addition to uncertainties regarding the dimensions measured, there was also laser-engraved identification on each specimen, which caused a slight overestimation of the volume and thus lowered the density. For comparison, three CVD SiC specimens with the same dimensions were measured. The average density was 3.17 g/cm³ or about 98.8% dense. For purposes of using in thermal conductivity calculation, the three samples in each direction were averaged: $\rho_{xs} = 2.792$ g/cm³; $\rho_{xy} = 2.860$ g/cm³; $\rho_z = 2.919$ g/cm³.
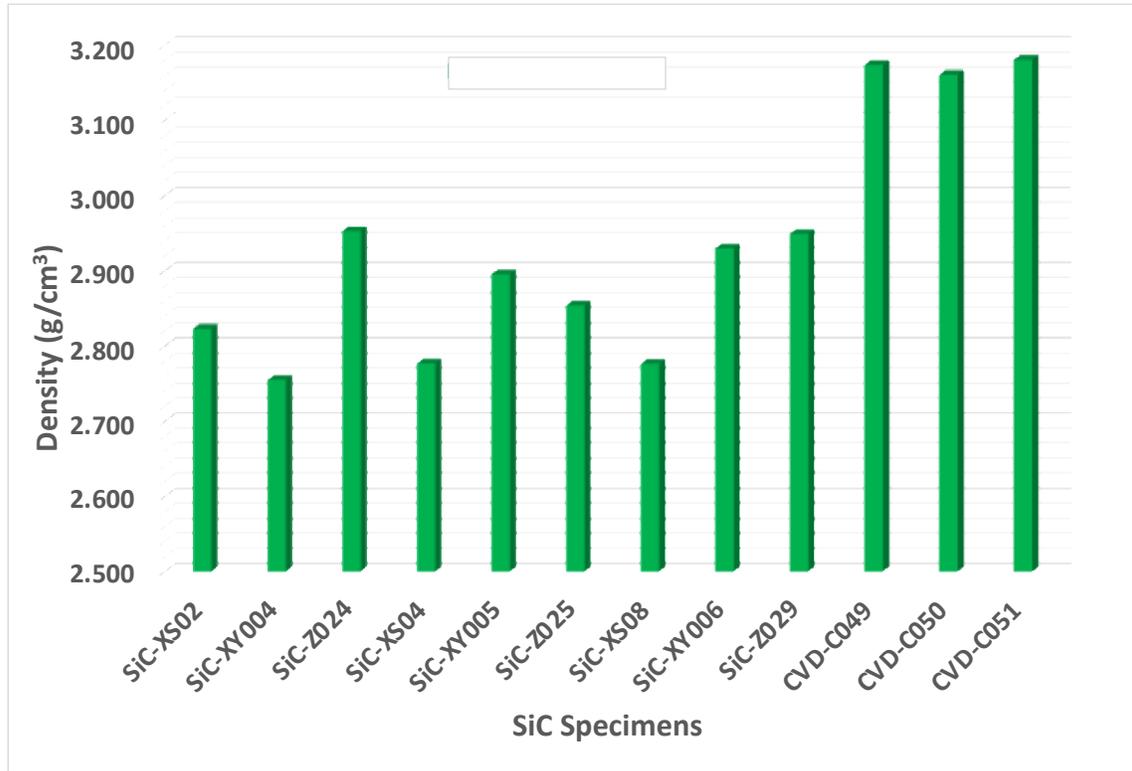
Figure 12. Density of 3D-printed SiC after CVI and CVD SiC.

4.3 Specific Heat Capacity

Specific heat capacity of the 3D-printed SiC was measured on Netzsch Pegasus 404C, a differential scanning calorimeter (DSC), following ASTM E1269 [23], from room temperature to 900 °C using a 10 °C/min heat/cooling rate. A ratio method includes a baseline run (two empty Pt pan/lid sets), a reference run with a sapphire standard, and a sample run. The specific heat of the sample, C_p, is calculated as follows:

$$C_p = \frac{DSC\ (sample-baseline)}{m_{sample}*HR*Sensitivity},$$
(Equation 6)

in which the DSC signal is in µV and HR is the heating rate; the sensitivity of the DSC is

$$Sensitivity = \frac{DSC\ (sapphire-baseline)}{m_{sapphire}*HR*C_p(sapphire)},$$
(Equation 7)

If we use the ratio between the specific heat capacities of the sample and reference sapphire, the sample C_p become independent of HR and sensitivity:

19

$$C_p = \frac{DSC\ (sample-baseline) * m_{sapphire}}{DSC\ (sapphire-baseline) * m_{sample}} C_p(sapphire), \qquad \text{(Equation 8)}$$

Figure 13 show the calculated C_p values of three SiC samples during heating and cooling. The scatter could be caused by sample-to-sample variations, baseline shifting, and radiation effects between the sapphire standard and SiC sample. The values for heating and one set of cooling curves are consistent with the literature [15]. The cooling data showed lower values, especially at high temperatures. A physics-based model is not used for curve fitting because of the lack of lower temperature (< 0 °C) data. The heating and cooling C_p curves are represented by 3rd order polynomials. Three curve-fitting results are plotted in Figure 14 along with the Handbook values for CVD SiC. The differences among the three directions were not as clear as thermal diffusivity. Since C_p is more sensitive to composition than microstructure, the scatter is likely due to sample variations and experimental uncertainty.
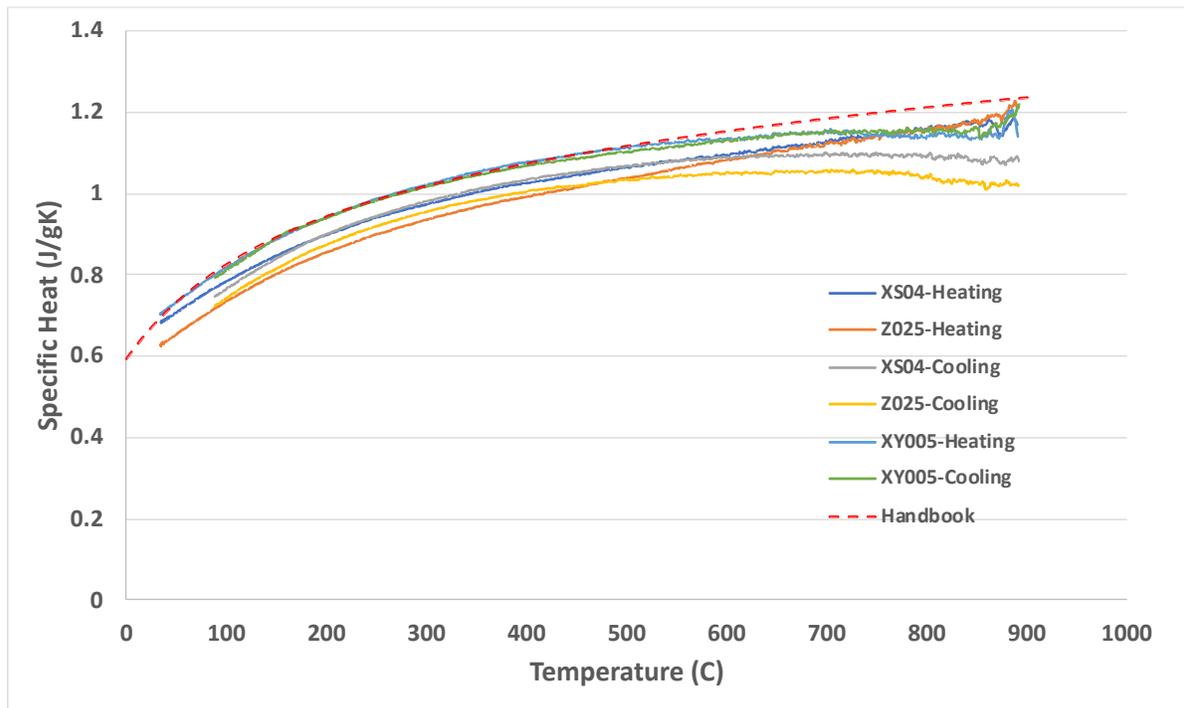
Figure 13. C_p vs temperature plots of three 3D-printed SiC samples during heating and cooling (SiC handbook values are represented by the dashed line).
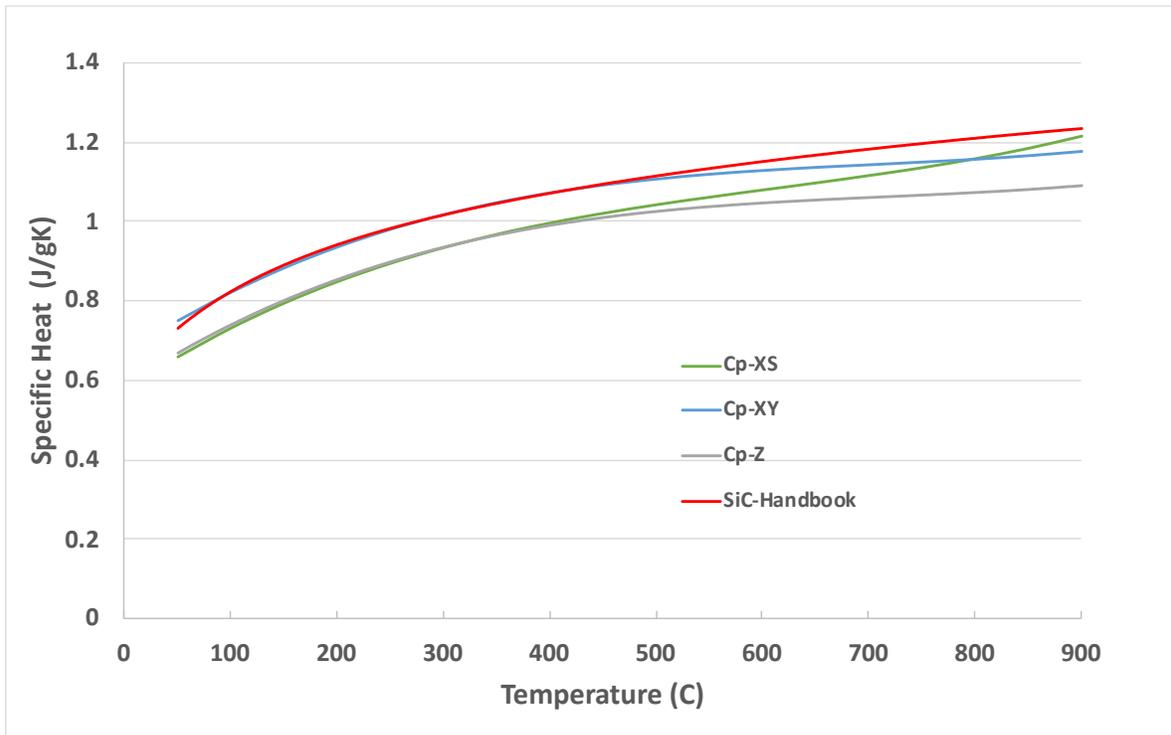
Figure 14. C_p (curve-fitting of heating data) in three printing directions compared with the reference data (Eq.10 in the SiC Handbook [15]).

4.4   Thermal Conductivity

The thermal conductivity of each of the materials was calculated using Equation 9 from the thermal diffusivity, density, and specific heat data which were measured and evaluated in the previous sections.

$$Thermal\ conductivity = Thermal\ Diffusivity \times Density \times Specific\ Heat, \qquad \text{(Equation 9)}$$

The average values in Figure 11were used for thermal diffusivity. The average measured densities for each direction were also used. The curve fit for C_p in Figure 14 was applied in Equation 9, and thermal conductivities of the three directions are shown in Figure 15.

21
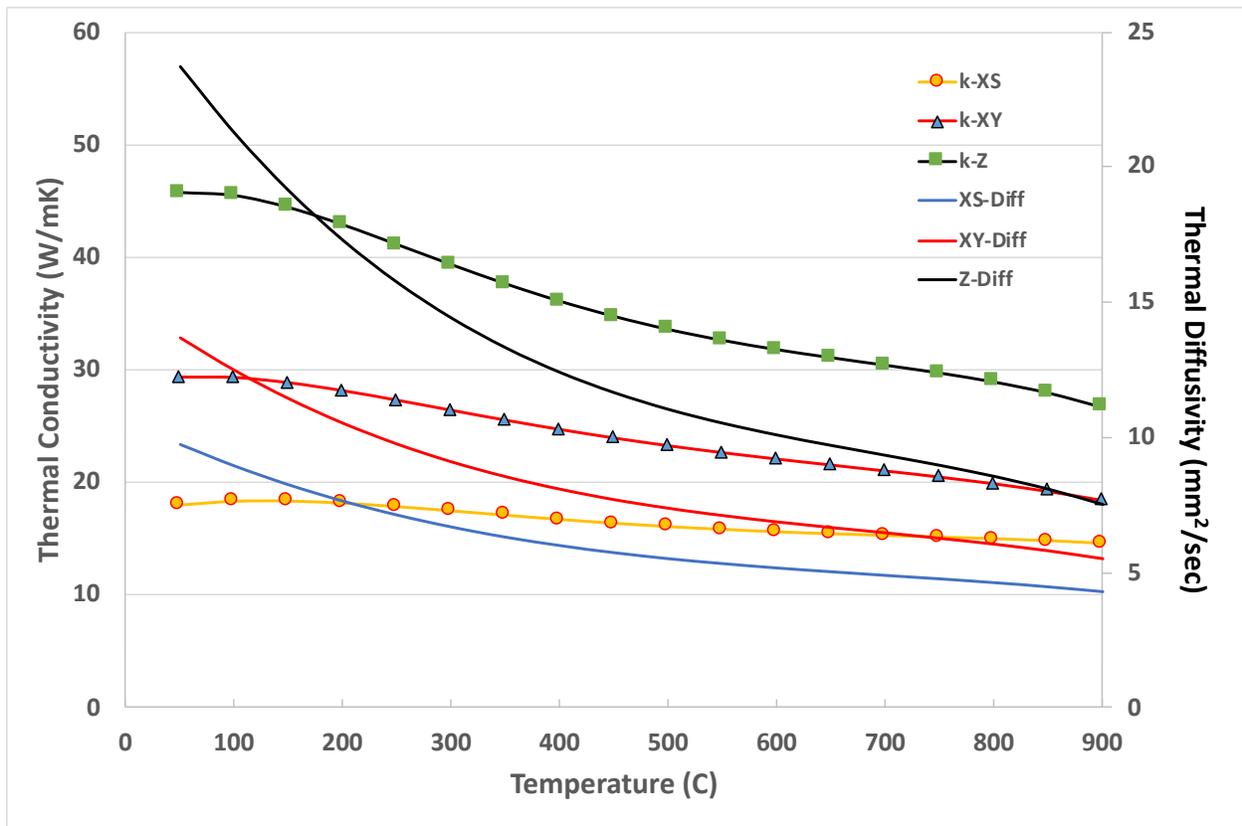
Figure 15. Thermal diffusivity and calculated thermal conductivity of three 3D-printed SiC samples with different orientation.

The calculated thermal conductivity showed a slower decline compared with the thermal diffusivity (plotted in the same graph) mainly because of three factors: (i) the increasing trend of Cp in the same temperature range; (ii) compared with thermal conductivity in the literature, 3D printed materials have lower thermal diffusivity (about 40–50% of CVD SiC), especially in the low temperature region. In some studies, the ambient Cp value was used along with the Dulong Petit limit, assuming Cp is a constant at high temperatures. Thus, the calculated thermal conductivity has the same steep decline from ambient to 400–500 °C.

4.5   Coefficient of Thermal Expansion

A Theta Dilatronic IX dual-push-rod differential dilatometer was used to measure the coefficient of thermal expansion (CTE) of nine specimens—three samples per each orientation. The samples were 10 mm in length and 6 mm in diameter. A NIST standard reference material (SRM) sapphire rod 10 mm was used. The system has 30 °C constant temperature controlled by a water bath as the reference temperature. The heating and cooling rates were the same at 3°C /min. The

22

alumina tube was evacuated three times and back filled with ultra-high purity (UHP) helium. The helium purge gas also passed through an oxygen gettering furnace (by CENTOR), and a flow rate of 5 mL/min was maintained throughout the measurements. Figure 16 shows the mean CTE vs temperature plots of all nine specimens. The CTE values increase from 2.5×10^{-6} K^{-1} at 70 °C to about 4.7×10^{-6} K^{-1} at 900 °C with little variations among specimens. The noise at low temperatures was due to the slow reaction of the furnace to follow the programmed heating rate. In general, CTE values after 100 °C become more stable. The measurements show that the temperature dependences in all nine samples were similar and the CTE did not show any change with respect to the printing orientation or Si doping. The average of the nine samples is also plotted and a logarithmic curve fit is used:

$$CTE = 0.9595 \, Ln \, (T) - 1.7681, \qquad \text{(Equation 10)}$$

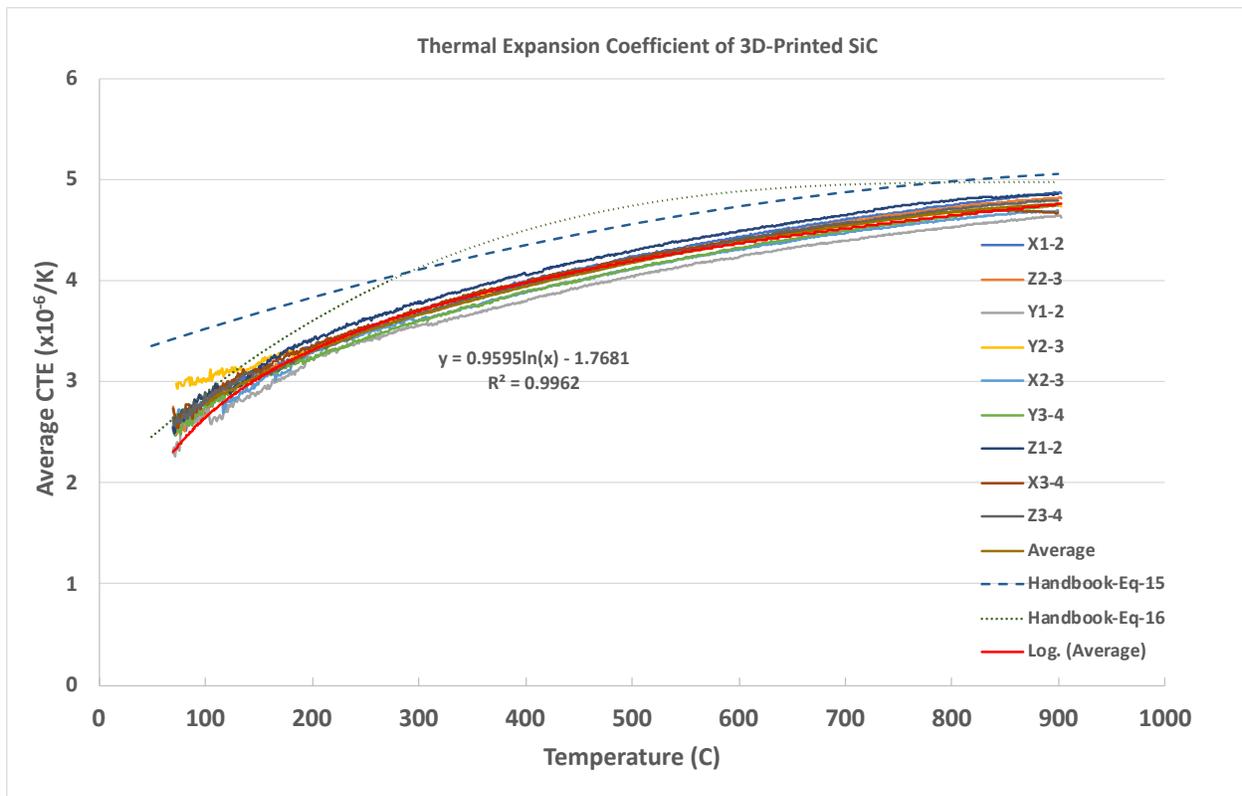in which T is temperature in °C and the R$_2$ value is 0.996.

Figure 16. Coefficient of thermal expansion (CTE) vs. temperature for nine printed SiC samples. The mean value curve equation for the nine samples with three different orientations is also given along with Eq. 15 and Eq. 16 in the SiC Handbook [15].

The CTE versus temperature curves from SiC Handbook [15] —equation (15) (3C-SiC in the range 277–1000 °C) and equation (16) (CVD 3C-SiC in the range -148–1000 °C) —are also plotted in Figure 16 which showed significant differences between the two types of 3C-SiC. The CTE results of SiC in this study exhibited lower values and also showed that thermal expansion of the 3D-printed material is independent of the printing process. The corresponding volume change upon heating for the TCR design and application can be considered constant in all directions.

5. RADIATION EFFECT STUDIES UNDERWAY

5.1 Neutron Irradiation Experiment

Neutron irradiation of six rabbit capsules has been carried out at HFIR to obtain the target displacement damage level of 2 dpa at three different temperatures (400, 650, and 900 °C). Irradiation has been already completed, and post-irradiation evaluation is being prepared. Mechanical testing after t neutron irradiation will be performed later in the fiscal year, and the results will be compared with the datasets presented in this report.

Each capsule contains 32 SiC disk specimens: 24 binderjet/CVI SiC disks and 8 CVD SiC disks, as shown in Table 6. Each of the first three capsules contains 24 3D-printed disk (Ø6 mm × 0.5 mm) specimens with XY orientation only, along with 8 CVD SiC disks. The second three capsules contain the same numbers of disks with Z orientation and CVD disks. In this test campaign, 84 disk specimens were tested before irradiation as reported here, and the majority of the 192 specimens listed in Table 6 will be tested at room temperature in the equibiaxial flexural loading condition to obtain failure strength data after irradiation. The same load frame in the Lamda facility, which was used for the baseline testing, will be used for this post-irradiation testing. Some of these irradiated disk specimens will also be used for thermal diffusivity measurement.

Table 6. SiC disk specimens in ongoing irradiation experiment

Capsule I.D.	Irradiation Temperature (°C)	# of 3D Print+CVI Disks (Orientation)	# of CVD Disks
SDTR01	400	24 (XY)	8
SDTR02	650	24 (XY)	8
SDTR03	900	24 (XY)	8
SDTR04	400	24 (Z)	8
SDTR05	650	24 (Z)	8
SDTR06	900	24 (Z)	8

5.2 Ion Irradiation Experiment

Ion irradiation is underway at the Ion Beam Materials Laboratory at the University of Tennessee, Knoxville, to obtain information on microstructural evolution during irradiation up to 40 dpa. The binderjet/CVI processed SiC and CVD SiC samples were irradiated with 5 MeV Si_{2+} ions at two target temperatures (400 and 650 °C) to three doses (2, 8, 40 dpa). Microstructural characterization is being conducted on some of the specimens that have already been irradiated using scanning electron microscopy (SEM), transmission electron microscopy (TEM), and scanning transmission electron microscopy (STEM).

Initial analysis was conducted on AM-SiC sample #XY082, which was irradiated at the lower irradiation temperature to a peak damage level of 40 dpa. Unirradiated and irradiated samples were prepared for TEM/STEM using standard dual-beam focused ion beam (FIB)/SEM lift-out techniques on either a FEI Quanta 3D FIB/SEM or a FEI Versa FIB/SEM equipped with Ga ions for milling. TEM/STEM analysis was done on a FEI Talos F200X STEM.

Large-scale porosity was observed in the SEM image in Figure 17 in the unirradiated region, although there was no qualitative difference in the porosity between the irradiated and unirradiated regions. The porosity appears to range in size up to ~20 μm, which is the approximate size of the feedstock powder and is consistent with reference [2]. The STEM images of the unirradiated region in Figure 18 show two large 6H-SiC particles around the CVI-SiC matrix. The CVI-SiC has columnar nanoscale grains and is highly faulted, likely by a combination of many of the structural polytypes of SiC. There is potentially some localized strain resulting from growth between particles and the matrix based on the strain contrast in Figure 18(b). Small nanoscale pores were also observed in the CVI that are much smaller than the pores found in the SEM image in Figure 17.
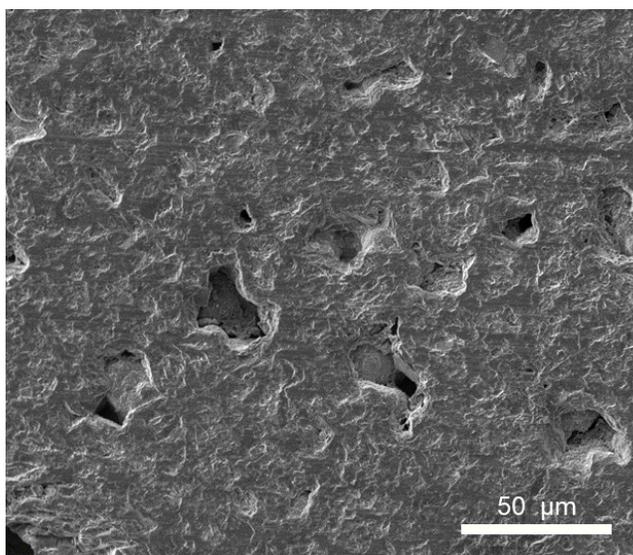

Figure 17. Secondary electron SEM image of the surface of the unirradiated region in the 3D-printed SiC sample #XY082.

Initial qualitative post-irradiation examination was conducted, as shown in Figure 19. As expected at this low irradiation temperature of ~400 °C, black spot damage consisting of nanometer-sized dislocation loops is the primary cause of the damage. There is a band of considerable damage at a depth of ~2–2.5 μm, consistent with 5 MeV Si_{2+} ion implantation. There appears to be more damage in the SiC particles than in the CVI-SiC matrix (likely due to the higher density of grain boundaries that act as defect sinks), although this could not be quantified at this time due the orientation of the lift-out relative to the relevant zone axes for imaging dislocation loops. Further characterization will be conducted to quantify the amount of damage in the particles, the matrix, and the interface region as a function of radiation dose and temperature and then compare the results directly with CVD-SiC.
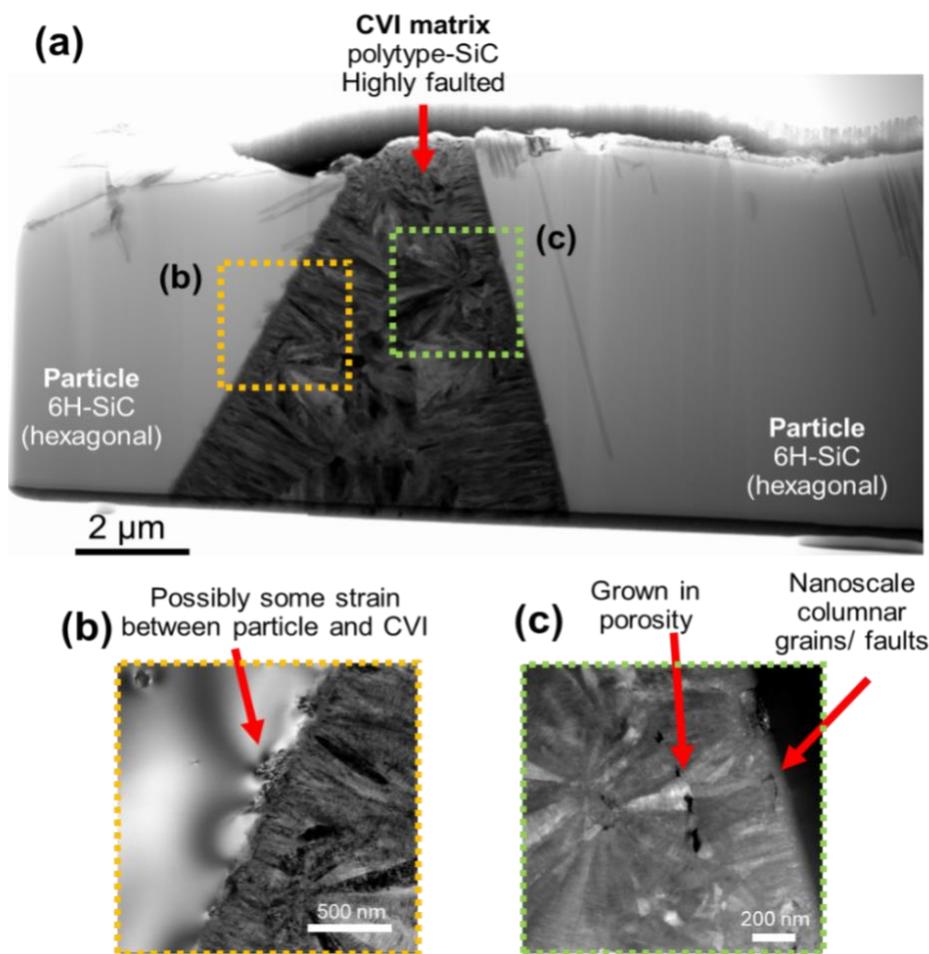

Figure 18: (a) STEM image of unirradiated 3D-printed SiC (from unirradiated part of XY082). (b) Strain contrast at the particle/matrix interface shows potential regions of localized strain. (c) STEM-HAADF image of CVI matrix showing columnar grains and grown-in porosity.
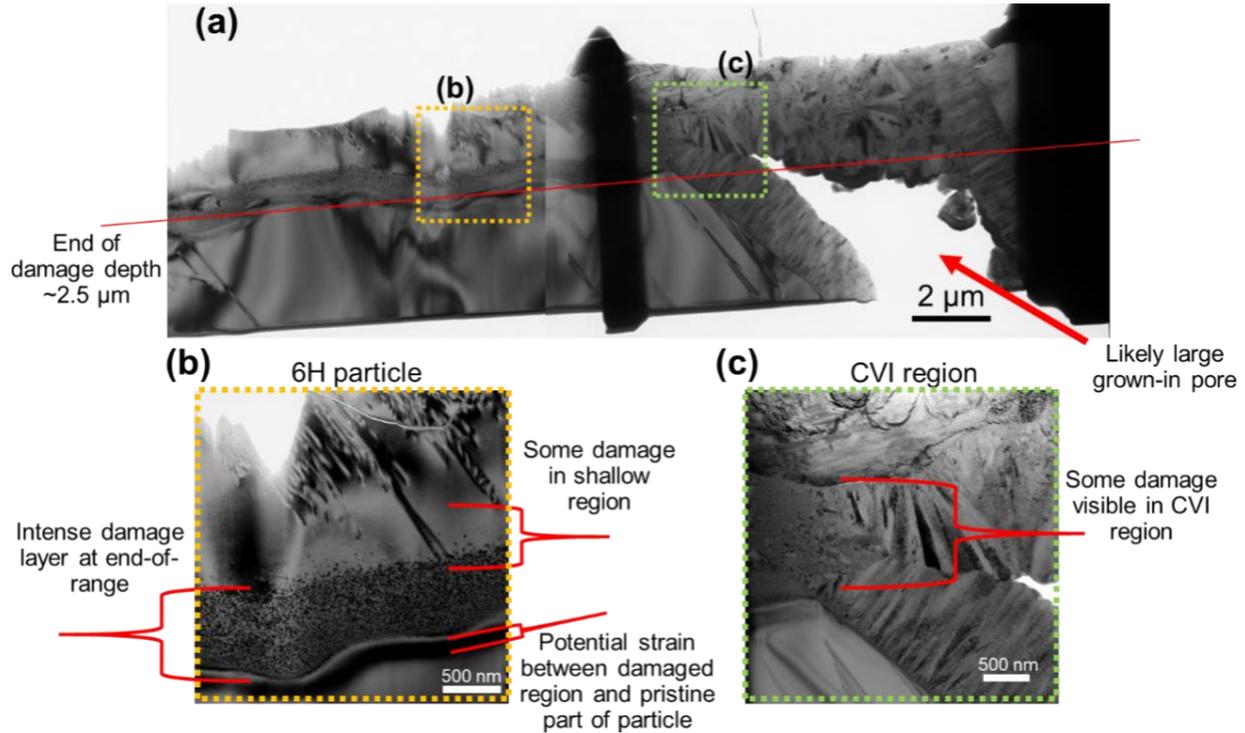
Figure 19: *(a) STEM image of AM-SiC irradiated at 400 °C to a dose of 40 dpa with 5 MeV Si2+ ions. (b) Highly damaged region of SiC particle with high concentration of black spots; above which there is a smaller amount of black spot damage. (c) Some damage accumulation is found in the CVI matrix, but this particular damage cannot be analyzed in detail because [1-210] or [1-100] zone axes could not be reached within the tilt range.*

6. SUMMARY AND CONCLUSIONS

Various mechanical and thermophysical tests were performed to evaluate the SiC materials produced by combined the processes of binderjet printing and CVI. The green SiC before CVI was also tested for tensile failure properties. Discussion was focused on the effects of specimen orientation on the mechanical and thermophysical properties. Summarized below are the key results and conclusions derived for each respective topical area.

Equibiaxial flexural strength data were measured for four different SiC materials consisting of three printed SiC materials and one CVD SiC. Although the mean failure strengths of the 3D-printed SiC were 22–27% lower than that of the reference material, CVD SiC, these values were still high (> 280 MPa). The Weibull moduli measured were within the range of 7–14, which is a typical range for SiC materials, and there was no evidence of different failure mechanisms between the binderjet plus CVI processed SiC and the reference SiC.

Green SiC tensile specimens of two different sizes and two orientations were produced using binderjet printing and were tested in uniaxial tension mode. The mean failure strength measured from the x-direction specimens was significantly lower than that of the y-direction specimens due to the deposition patterns. Weibull analysis of the specimens for the two sizes showed typical size effects: the measured Weibull moduli and failure strengths for the larger specimens were higher for most of the compared datasets.

The thermophysical properties of 3D-printed SiC after CVI were measured in three principal directions on multiple specimens. The measurements showed that specific heat and thermal expansion data are not sensitive to the build direction and are in agreement with what was observed in the reference CVD SiC, while thermal diffusivity is highly dependent on the build direction and can be correlated to the anisotropic microstructures of the 3D-printed SiC. To facilitate application of this information on the design and analysis of the TCR core, empirical trendlines were generated on theses experimentally determined results.

7. REFERENCES

[1] K.G. Field, J. Simpson, M.N. Gussev, H. Wang, M. Li, X. Zhang, X. Chen, T. Koyanagi, K. Kane, A. Marquez Rossy, M. Balooch, K.A. Terrani, Handbook of advanced manufactured material properties from TCR structure builds at ORNL – FY19, Oak Ridge, 2019. https://doi.org/M3CT-19OR06090121.

[2] K. Terrani, B. Jolly, M. Trammell, 3D printing of high-purity silicon carbide, J. Am. Ceram. Soc. 103 (2020) 1575–1581. https://doi.org/10.1111/jace.16888.

[3] Y. Katoh, L.L. Snead, C.H. Henager, T. Nozawa, T. Hinoki, A. Iveković, S. Novak, S.M. Gonzalez de Vicente, Current status and recent research achievements in SiC/SiC composites, J. Nucl. Mater. 455 (2014) 387–397. https://doi.org/https://doi.org/10.1016/j.jnucmat.2014.06.003.

[4] K.A. Terrani, C. Ang, L.L. Snead, Y. Katoh, Irradiation stability and thermo-mechanical properties of NITE-SiC irradiated to 10 dpa, J. Nucl. Mater. 499 (2018) 242–247. https://doi.org/https://doi.org/10.1016/j.jnucmat.2017.11.040.

[5] L.L. Snead, Y. Katoh, T. Nozawa, Radiation Effects in SiC and SiC–SiC, in: R.J.M. Konings (Ed.), Compr. Nucl. Mater., Elsevier, Oxford, 2012: pp. 215–240. https://doi.org/https://doi.org/10.1016/B978-0-08-056033-5.00093-8.

[6] Y. Katoh, N. Hashimoto, S. Kondo, L.L. Snead, A. Kohyama, Microstructural development in cubic silicon carbide during irradiation at elevated temperatures, J. Nucl. Mater. 351 (2006) 228–240. https://doi.org/https://doi.org/10.1016/j.jnucmat.2006.02.007.

[7] Y. Katoh, K. Ozawa, C. Shih, T. Nozawa, R.J. Shinavski, A. Hasegawa, L.L. Snead, Continuous SiC fiber, CVI SiC matrix composites for nuclear applications: Properties and irradiation effects, J. Nucl. Mater. 448 (2014) 448–476. https://doi.org/https://doi.org/10.1016/j.jnucmat.2013.06.040.

[8] S. Kondo, Y. Katoh, L.L. Snead, Concentric ring on ring test for unirradiated and irradiated

miniature SiC specimens, J. Nucl. Mater. 417 (2011) 406–410. https://doi.org/https://doi.org/10.1016/j.jnucmat.2010.12.083.

[9]   K.A. Terrani, J.O. Kiggans, C.M. Silva, C. Shih, Y. Katoh, L.L. Snead, Progress on matrix SiC processing and properties for fully ceramic microencapsulated fuel form, J. Nucl. Mater. 457 (2015) 9–17. https://doi.org/https://doi.org/10.1016/j.jnucmat.2014.10.034.

[10] K.A. Terrani, J.O. Kiggans, Y. Katoh, K. Shimoda, F.C. Montgomery, B.L. Armstrong, C.M. Parish, T. Hinoki, J.D. Hunn, L.L. Snead, Fabrication and characterization of fully ceramic microencapsulated fuels, J. Nucl. Mater. 426 (2012) 268–276. https://doi.org/https://doi.org/10.1016/j.jnucmat.2012.03.049.

[11] J. Simpson, J. Haley, C. Cramer, O. Shafer, A. Elliott, W. Peter, L. Love, R. Dehoff, Considerations for Application of Additive Manufacturing to Nuclear Reactor Core Components, Oak Ridge, 2019. https://doi.org/ORNL/TM-2019/1190 M3CT-19OR06090123.

[12] P. Champlin, J. Burns, C. M. Petrie, X. Hu, K. D. Linton, R. Howard, K. A. Terrani, Capsule and Specimen Geometries for HFIR Irradiation Testing Supporting the Transformational Challenge Reactor, ORNL/TM-2019/1310 (M3CT-19OR06090120), Oak Ridge National Laboratory, 2019. https://doi.org/M3CT-19OR06090121.

[13] ASTM C1499 − 09 (Reapproved 2013): Standard Test Method for Monotonic Equibiaxial Flexural Strength of Advanced Ceramics at Ambient Temperature.

[14] W. Weibull, A statistical distribution function of wide applicability, Journal of Applied Mechanics, 18 (3) (1951) 293–297.

[15]   L.L. Snead, T. Nozawa, Y. Katoh, T. S. Byun, S. Kondo, D.A. Petti, Handbook of SiC properties for fuel performance modeling, J. Nucl. Mater. 371 (2007) 329–377. https://doi.org/https://doi.org/10.1016/j.jnucmat.2007.05.016.

[16] S.G. Hong, T.S. Byun, R.A. Lowden, L.L. Snead, Y. Katoh, Evaluation of the Fracture Strength for SiC Layers in the TRISO-coated Fuel Particle, J. of the Amer. Ceramics. Soc. 90 (2007) 184-191.

[17] T. S. Byun, E. Lara-Curzio, L. L. Snead, Y. Katoh, Miniaturized Fracture Stress Tests for Thin-Walled Tubular SiC Specimens, J. of Nucl. Mater. 367-370 (2007) 653-658.

[18] ASTM E1461-07, Standard Test Method for Thermal Diffusivity by the Flash Method, ASTM International, West Conshohocken, PA, 2007.

[19] W.J. Parker, R.J. Jenkins, C.P. Butler, and G.L. Abbott, J. Appl. Phys. 32, 1679 (1961).

[20] R.D. Cowan, Pulse Method of Measuring Thermal Diffusivity at High Temperatures, Journal of Applied Physics 34(4) (1963) 926-927.

[21] L.M. Clark III, R.E. Taylor, Radiation loss in the flash method for thermal diffusivity, Journal of Applied Physics 46(2) (1975) 714-719.

[22] Goldberg Yu., Levinshtein M.E., Rumyantsev S.L. in *Properties of Advanced SemiconductorMaterials GaN, AlN, SiC, BN, SiC, SiGe*. Eds. Levinshtein M.E., Rumyantsev S.L., Shur M.S., John Wiley & Sons, Inc., New York, 2001, 93-148.

[23] ASTM E1269-11, Standard Test Method for Determining Specific Heat Capacity by Differential Scanning Calorimetry, ASTM International, West Conshohocken, PA, 2018.